Radio frequency wave interactions with a plasma sheath: The role of wave and plasma sheath impedances

著者	Myra J. R., Kohno H.
journal or publication title	Physics of Plasmas
volume	26
number	5
page range	052503-1-052503-14
year	2019-05-08
URL	http://hdl.handle.net/10228/00007255

doi: info:doi/10.1063/1.5088343

Radio frequency wave interactions with a plasma sheath: the role of wave and plasma sheath impedances

J.R. Myra[1] and H. Kohno[2] †

[1] *Lodestar Research Corporation, 2400 Central Avenue, Boulder, Colorado 80301, USA*
[2] *Department of Mechanical Information Science and Technology, Kyushu Institute of Technology,680-4 Kawazu, Iizuka, Fukuoka 820-8502, Japan*

Abstract

Radio frequency (RF) sheaths form near surfaces where plasma and strong RF fields coexist. The effect of these RF sheaths on wave propagation near the boundary can be characterized by an effective sheath impedance that includes both resistive and capacitive contributions describing RF sheath rectification and RF power absorption in the sheath [J. R. Myra and D. A. D'Ippolito, Phys. Plasmas **22**, 062507 (2015)]. Here we define a dimensionless parameter, the ratio of incoming wave impedance to the sheath impedance, which determines the characteristics of the interaction, ranging from quasi-conducting to quasi-insulating, or in the case of matched impedances, to either perfect absorption or a sheath-plasma resonance. A semi-analytical analysis is carried out for electrostatic slow waves in the ion cyclotron range of frequencies (ICRF). For the propagating slow wave case, where the incident wave is partially reflected, the fraction of power dissipated in the sheath is calculated. For the evanescent slow wave case, which admits a sheath-plasma resonance, an amplification factor is calculated. Using the impedance ratio approach, RF sheath interactions are characterized for a range of RF wave and plasma parameters including plasma density, magnetic field angle with respect to the surface, wave frequency and wave-vector components tangent to the surface. For a particularly interesting example case, results are compared with the rfSOL code [H. Kohno and J. R. Myra, Comput. Phys. Commun. **220**, 129 (2017)]. Finally electromagnetic effects, absent from the semi-analytical analysis, are assessed.

Keywords: radio frequency, ICRF, sheath, impedance, tokamak

† present address: Department of Physics and Information Technology, Kyushu Institute of Technology, 680-4 Kawazu, Iizuka, Fukuoka 820-8502, Japan

I. Introduction

Radio frequency (RF) waves in the ion cyclotron range of frequencies (ICRF) can provide a cost-effective and flexible means of heating and driving current in present day and future tokamak devices. However, in some operational regimes unwanted interactions occur in places where intense RF waves, plasma and material surfaces coexist. These interactions include the formation of high voltage "rectified" RF sheaths and excessive surface power dissipation. The former is associated with increased ion impact energies on the surface resulting in sputtering of impurities; the latter may result in excessive erosion and material damage. These ICRF edge and wall interactions have been studied in the fusion environment for many years as reviewed in Refs. [1, 2]. They have also been investigated in recent experiments on many tokamaks,[3-10] and linear test stands[11,12] and they have been the subject of a number of dedicated modeling efforts.[13-20]

Since RF sheaths are thought to play a central role in understanding the observations, developing models for sheaths and their interaction with RF waves is an important aspect of the work and is the subject of the present paper. The RF sheaths themselves exist on small spatial scales perpendicular to the surface, on the order of a few to perhaps 10 or 20 Debye lengths. Since this scale is much smaller than RF wavelengths of interest, and certainly much smaller than the global scale of a whole tokamak, RF sheath effects have typically been included in global wave simulation codes using a sheath boundary condition (BC) which may be understood in terms of an effective surface impedance.[21,22] In the limit of high frequencies relative to the ion plasma frequency, an RF sheath is dominantly capacitive and the effective surface impedance, i.e. the sheath impedance, is therefore imaginary and scales inversely with the wave frequency. For very large RF voltages driving the sheath, the sheath width and the impedance become large and the sheath behaves as if it were quasi-insulating,[13,18] a limit which has also been referred to as the "wide sheath limit." Quasi-conducting and intermediate limits are also possible, including that of the sheath-plasma resonance.[23-25] It is of interest to know *a priori*, based on plasma and wave parameters, when various limiting cases can be expected and how one might broadly characterize the wave interaction with an RF sheath over a range of these plasma and wave parameters. That is the goal of the present paper.

The response of the wave to the sheath depends on both the surface impedance provided by the sheath and an effective wave impedance. The ratio of these two impedances is what actually controls whether the behavior is quasi-conducting, quasi-insulating, intermediate, or resonant. The sheath impedance itself,[26] denoted z_s, has been studied in previous publications. A Debye-scale physics model[21] was employed to parametrize the sheath impedance in terms of analytical functions and numerical fits.[22] The result is a dimensionless function of the form

This manuscript was accepted by Phys. Plasmas. Click here to see the version of record.

$\hat{z}(\hat{\omega},\hat{\Omega},b_n,\xi)$ where the dimensionless $\hat{z}$ is related to the dimensional sheath impedance in Gaussian (z_s) and SI ($z_{s,SI}$) units as follows

$$\hat{z}(\hat{\omega},\hat{\Omega},b_n,\xi)=\frac{\varepsilon_0\omega_{pi}}{\lambda_d}z_{s,SI}=\frac{\omega_{pi}}{4\pi\lambda_d}z_s \tag{1}$$

In the remainder of this paper, Gaussian CGS units will be employed; however, the important quantities are in any case dimensionless ratios. Here the dimensionless inputs are given by $\hat{\omega} = \omega/\omega_{pi}$, $\hat{\Omega} = \Omega_i/\omega_{pi}$, $b_n = \mathbf{s}\cdot\mathbf{b}$ and the absolute value of the normalized RF sheath voltage $\xi = e|V_{rf}|/T_e$. The RF wave is proportional to $\exp(i\mathbf{k}\cdot\mathbf{x}-i\omega t)$ where ω is the wave frequency and $\mathbf{k}$ is the wave-vector; Ω_i is the ion cyclotron frequency and ω_{pi} is the ion plasma frequency. The magnetic field direction $\mathbf{b}$ is at an oblique angle to the unit normal to the surface $\mathbf{s}$, and b_n is the component of $\mathbf{b}$ directed into or out of the surface. (To avoid confusion with the index of refraction, we use $\mathbf{s}$ instead of $\mathbf{n}$ for the surface normal.) In the present paper, we employ the function $\hat{z}(\hat{\omega},\hat{\Omega},b_n,\xi)$ from Ref. 22 as given and concentrate on the implications for wave reflection, absorption and amplification at the sheath surface.

The scale separation implicit in defining a sheath BC is valid for $\Delta << \lambda_{rf}$ where Δ is a measure of the RF sheath width and λ_{rf} is the RF wavelength. Within this approximation, the Debye-scale model determining $\hat{z}$ contains a rich amount of physics, including the effect, on the RF waves, of plasma profiles and any wave resonances within the magnetic and non-neutral regions of the sheath. An example, discussed in Ref. 22 (see Fig. 2 and the associated discussion therein) is the ion plasma resonance, which for the illustrated sheath parameters is the remnant of the lower hybrid resonance in the non-neutral sheath. (See also Fig. 2 of the present paper.) We emphasize that although the present paper, in order to obtain analytic insight, will employ constant plasma parameters *in the plasma volume* (i.e. the region explicitly modeled in Fig. 1), the sheath impedance model yielding $\hat{z}(\hat{\omega},\hat{\Omega},b_n,\xi)$ is more general and takes into account plasma profile variations *within the sheath*.[21] The physical model within the sheath is electrostatic, justified by the short spatial Debye-length scales.

A significant limitation of the RF wave and sheath interaction model discussed in this paper is that the RF waves in the plasma volume are restricted to slow waves in the electrostatic limit (except for electromagnetic effects treated briefly in Sec. VI). RF antennas dominantly launch the fast wave; however, perfect fast wave polarization of the RF fields in the tokamak edge plasma is unachievable in practice. The slow wave component is generally believed to be responsible for RF sheath interactions, whether created directly by the antenna[3,4] (e.g. due to misalignment or the parasitic effect of septa and limiters), or indirectly in the far field by conversion of fast waves to slow waves caused by interaction with non-flux-surface conforming

This manuscript was accepted by Phys. Plasmas. Click here to see the version of record.

walls.[16,27] The former case is usually associated with sheaths that are magnetically connected to the antenna; the latter with sheaths that are not magnetically connected. Both cases have been observed experimentally and are discussed in Ref. 10. The model in this paper applies straightforwardly to the magnetically connected case. It may also be a useful guide in the case of fast-to-slow wave conversion at the sheath surface, provided that the dominant wavevector of the slow wave can be estimated. (See e.g. Refs. 19 and 27 for relevant considerations.)

A more complete treatment, directly embedding the possibility of fast-to-slow wave conversion, would require a substantial, and necessarily electromagnetic, generalization of the present work. Although the fundamental equations can be written down, analytical progress seems to be elusive, and a fully numerical approach comes at the cost of loss of intuition and analytical transparency. In principle, although some important details are different, the more complete treatment should be equivalent to the calculation of the connection coefficients already discussed in Ref. 16, i.e. the "output" (outgoing) fast and slow wave amplitudes resulting from given "input" (incoming) fast or slow wave amplitudes.

The plan of our paper is as follows. The geometry of our model and the analytical theory leading to the definition of wave impedance, or its inverse the wave admittance, are given in Sec. II. The coefficients that describe reflection, absorption and amplification of the incoming slow wave are also obtained. Some important qualitative properties of the variation of z_s with wave and plasma parameters concludes Sec II B. In Sec. III we present basic wave physics for the electrostatic slow wave (SW) together with a numerical example illustrating the procedure employed in the rest of the paper. Sec. IV presents the variations of the wave response with density, magnetic field strength and angle, RF frequency and wavenumber. In Sec V comparison is made of the present theory with a result from rfSOL. The rfSOL code is a finite-element code with Eq. (1) implemented in a sheath boundary condition.[25,28] In Sec. VI electromagnetic effects are briefly considered. Although an analytical electromagnetic theory is not presented in this paper, numerical results show that the present electrostatic theory captures the correct qualitative behavior. Finally a summary and conclusions are given in Sec. VII. Some details of the calculations are deferred to the appendices: Appendix A discusses the relationship between the incident and reflected wave admittances; Appendices B and C establish power balance identities for propagating and evanescent waves, respectively; and Appendix D provides details of the electromagnetic calculation used in Sec. VI.

II. Geometry and model problem

A. Basic geometry and wave impedance theory

The geometry under consideration is shown in Fig. 1. An important quantity is the magnetic field angle with respect to the surface, φ, given by tan φ = B_x/B_y. The tangential (t) direction on the sheath surface is in the y-z plane. We regard k_y and k_z as inputs, and use the dispersion relation to obtain k_x. For the electrostatic SW model, there will be two roots, one incoming (denoted $\mathbf{k}_1$) and one outgoing (denoted $\mathbf{k}_2$). For propagating waves, the determination of incoming and outgoing requires an analysis of the group velocity v_{gx}. Incoming propagating modes have Re $v_{gx1} > 0$. In the case of evanescent modes the incoming branch must satisfy Im $k_{1x} > 0$

Assuming for brevity a unit amplitude incoming wave (final results will not depend explicitly on the amplitude), the electrostatic potential takes the form

$$\Phi = (e^{ik_{1x}x} + Ae^{ik_{2x}x})e^{i\mathbf{k}_t\cdot\mathbf{x}-i\omega t} \tag{2}$$

where $\mathbf{k}_1 = (k_{1x}, k_y, k_z)$ is incoming, $\mathbf{k}_2 = (k_{2x}, k_y, k_z)$ is outgoing and $\mathbf{k}_t$ = (0,k_y, k_z) is common to both. Here the subscript "t" denotes the tangential component to the surface. The amplitude A is unknown at this stage. The sheath boundary condition is[21]

$$\mathbf{E}_t = \nabla_t\left(\frac{\omega z_s}{4\pi i}\mathbf{s}\cdot\mathbf{D}\right) \tag{3}$$

where the unit normal pointing from the surface into the plasma is $\mathbf{s} = -\mathbf{e}_x$ and $\mathbf{D} = \bar{\bar{\varepsilon}}\cdot\mathbf{E}$ with cold-fluid dielectric tensor $\bar{\bar{\varepsilon}}$.

Using Eq. (2) and choosing x = 0 to be the location of the sheath-plasma interface where the sheath BC is to be applied[21] we have

$$\mathbf{E}_t = -i\mathbf{k}_t(1+A) \tag{4}$$

The total electric field at the sheath, suppressing the exp(i$\mathbf{k}_t\cdot\mathbf{x}$–iωt) dependence, is

$$\mathbf{E} = -i\mathbf{k}_1 e^{ik_1x} - i\mathbf{k}_2 A e^{ik_2x} \tag{5}$$

The sheath BC may be written as

$$(1+A) = \frac{\omega z_s}{4\pi}\mathbf{s}\cdot\bar{\bar{\varepsilon}}\cdot(\mathbf{k}_1 + \mathbf{k}_2 A) \tag{6}$$

which determines A, the amplitude of the reflected wave. Explicitly

This manuscript was accepted by Phys. Plasmas. Click here to see the version of record.

$$A = -\frac{\rho_1 - 1}{\rho_2 - 1} \tag{7}$$

where

$$\rho_j = \frac{\omega z_s}{4\pi}\mathbf{s}\cdot\bar{\bar{\varepsilon}}\cdot\mathbf{k}_j \equiv \frac{z_s}{z_{wj}} = z_s y_{wj} \tag{8}$$

Here z_{wj} is defined as the wave impedance corresponding to wave-vector $\mathbf{k}_j$ (j = 1,2), and its inverse $y_{wj} = 1/z_{wj}$ is the wave admittance. When discussing properties of the wave admittance y_w for general values of $\mathbf{k}$, the index j will be suppressed in the following.

From Eq. (7) several main features are already evident. For $|\rho_j| << 1$ (negligible sheath impedance seen by the waves) one obtains A = –1 and the sheath BC behaves like a perfectly conducting wall BC. For $|\rho_j| >> 1$ (large sheath impedance) the result is $A = -\rho_1/\rho_2$. If, in addition to being large, $\rho_1 = -\rho_2$ as it will be for the case of a perpendicular magnetic field ($|b_n| = 1$) the sheath BC behaves like an insulating BC (i.e. A = 1). For $\rho_1 = 1$ (A = 0) the waves are perfectly absorbed by the sheath (impedance matching) and for $\rho_2 = 1$ ($A = \infty$) we encounter a resonance (the sheath-plasma resonance). Finally for |A| = 1 it will be shown that there is no power absorption of the incoming Poynting flux by the sheath.

This completes the definition of the wave admittance as

$$y_w = \frac{\omega}{4\pi}\mathbf{s}\cdot\bar{\bar{\varepsilon}}\cdot\mathbf{k} \tag{9}$$

Since the total current in the plasma (including displacement current) is

$$\mathbf{J} = \frac{\omega}{4\pi i}\mathbf{D} = -\frac{\omega}{4\pi}\bar{\bar{\varepsilon}}\cdot\mathbf{k}\ \Phi \tag{10}$$

the wave admittance for a single plane wave, with current density and potential given by **J** and Φ, is simply

$$y_w = \frac{J_x}{\Phi} \tag{11}$$

To proceed further we introduce the dielectric tensor

$$\bar{\bar{\varepsilon}} = \varepsilon_\perp\bar{\bar{I}} + (\varepsilon_{||} - \varepsilon_\perp)\mathbf{bb} + i\varepsilon_\times\mathbf{b}\times\bar{\bar{I}} \tag{12}$$

which yields the admittance of a plane wave with wave-vector $\mathbf{k}$ in the present geometry as

$$y_w = -\frac{\omega}{4\pi}[\varepsilon_\perp k_x + (\varepsilon_\parallel - \varepsilon_\perp) b_x k_\parallel + i\varepsilon_\times \mathbf{e}_x \cdot \mathbf{b}\times\mathbf{k}] \tag{13}$$

Here, **b** = **B**/B, and for applications to ICRF we may take $\varepsilon_\perp = 1 + \omega_{pi}^2/(\Omega_i^2 - \omega^2)$, $\varepsilon_\parallel = 1 - \omega_{pe}^2/\omega^2$ and $\varepsilon_\times = \omega_{pi}^2\omega/\Omega_i(\omega^2 - \Omega_i^2)$. In the present paper, we will only consider a plasma with a single ion species, taken to be deuterium, although the expressions up to Eq. (13) are general in this respect.

B. Qualitative behavior of the sheath impedance

Since the parametric dependence of z_s will play a role in the results of this paper, it is important to understand some of those basic properties qualitatively. Figure 2 shows the results of a scan in $\hat{\omega}$, which is quite instructive in this regard. Considering first the small $\hat{\omega}$= ω/ω_{pi} (high density) limit, as the density n_e rises, Im $\hat{z}$ typically falls. The reason is because of smaller λ_d and hence smaller RF sheath width Δ that controls the capacitive contribution $\propto i\Delta/\omega$. On the other hand, for large n_e the particle currents, in particular the electron current, becomes more important than the displacement current. Because the electron current is in phase with the RF voltage, this results in large Re $\hat{z}$. At low density, large $\hat{\omega}$ (i.e. the right end of the plot), the converse is true: the capacitive contribution dominates, but it decreases with increasing wave frequency causing Im $\hat{z}$ to decrease; the resistive electron contribution decreases with n_e causing Re $\hat{z}$ to decrease with $\hat{\omega}$.

The RF amplitude ξ is also an important parameter (not illustrated). As ξ increases, z_s generally increases[22] (because of a wider sheath, and hence larger Δ) which implies a longer distance for particles and displacement current to traverse. Hence, as T_e rises at fixed V_{rf}, ξ will drop causing z_s to drop.

Thus at low n_e and T_e and high V_{rf} the sheath is most likely to be in the quasi-insulating "wide sheath" limit. Conversely, at high n_e and T_e and moderate V_{rf} the sheath is more likely to be in the conducting limit. However, as we shall see, the wavenumber and frequency of the RF and other factors such as impact angle of the magnetic field play an important role as well.

III. Dispersion relation, group velocity and Poynting flux

A. Theory

For the model geometry we have $k_\parallel = k_x b_x + k_y b_y$, $k_\perp^2 = k^2 - k_\parallel^2$ and in this section we assume **k** is pure real since we are concerned with the propagation properties. The electrostatic slow wave dispersion relation is[30]

$$\mathcal{D}(\omega, k_x) = k_\perp^2 \varepsilon_\perp + k_\parallel^2 \varepsilon_\parallel = 0 \tag{14}$$

This manuscript was accepted by Phys. Plasmas. Click here to see the version of record.

and the group velocity is

$$\mathbf{v}_g = \frac{\partial\omega}{\partial\mathbf{k}} = -\frac{\partial\mathscr{D}/\partial\mathbf{k}}{\partial\mathscr{D}/\partial\omega} \tag{15}$$

After some manipulation we find

$$\mathbf{v}_g = -\frac{1}{G}(\varepsilon_\perp \mathbf{k}_\perp + \varepsilon_{||} k_{||}\mathbf{b}) = -\frac{1}{G}[\varepsilon_\perp \mathbf{k} + (\varepsilon_{||} - \varepsilon_\perp)k_{||}\mathbf{b}] = -\frac{1}{G}\mathrm{Re}\,\bar{\bar{\varepsilon}}\cdot\mathbf{k} \tag{16}$$

where

$$G = \frac{1}{2}\frac{\partial D}{\partial\omega} = \frac{k_\perp^2\omega_{pi}^2\omega}{(\omega^2-\Omega_i^2)^2} + \frac{k_{||}^2\omega_{pe}^2}{\omega^3} \tag{17}$$

The x-component, v_{gx}, is of particular interest for determining the incoming and outgoing roots. It is given by

$$v_{gx} = -\frac{1}{G}[\varepsilon_\perp k_x + (\varepsilon_{||} - \varepsilon_\perp)k_{||}b_x] = \frac{4\pi}{\omega}\frac{\mathrm{Re}\,y_w}{G} \tag{18}$$

The denominator obeys $G > 0$ for all situations of interest (propagating waves, i.e. $\mathbf{k}$ pure real). The numerator, Re y_w, can have either sign. For example, when $b_z = b_y = 0$, $b_x = 1$ (perpendicular case) $v_{gx} = -k_x\varepsilon_{||}/G$ and it follows that v_{gx} has the same sign as k_x, i.e. the wave is a forward wave. However, when $b_z = 1$, $b_x = b_y << 1$ (glancing case) and $k_{||}$ is sufficiently small, $v_{gx} = -k_x\varepsilon_\perp/G$; propagation occurs when $\varepsilon_\perp > 0$ (tenuous plasma) therefore v_{gx} has the opposite sign from k_x, i.e. the wave is a backward wave. These conditions for forward and backward propagation of the SW are well known.

The Poynting flux is[30]

$$\mathbf{S} = \frac{c}{16\pi}\mathbf{E}^*\times\mathbf{B}_1 + \mathrm{cc} \tag{19}$$

cc implies complex conjugate and $\mathbf{B}_1$ is the RF magnetic field perturbation. In the electrostatic limit we cannot use $\mathbf{B}_1 = \mathbf{n}\times\mathbf{E}$, where $\mathbf{n} = \mathbf{k}c/\omega$, but instead must work to higher order in the electrostatic approximation. From $\mathbf{n}\times\mathbf{B}_1 = -\mathbf{D}$, crossing with $\mathbf{n}$ and using $\mathbf{n}\cdot\mathbf{B}_1 = 0$ we find

$$\mathbf{B}_1 = \frac{1}{n^2}\mathbf{n}\times\mathbf{D} \tag{20}$$

This manuscript was accepted by Phys. Plasmas. Click here to see the version of record.

Note that this is not zero, but is indeed smaller by $\left|\overline{\overline{\varepsilon}}/n^2\right|$ than the $\mathbf{n}\times\mathbf{E}$ estimate, where n >> 1 applies in the electrostatic approximation. Combining and employing $\mathbf{E} = -i\mathbf{k}\Phi$ where we consider a single plane wave (either $\mathbf{k}_1$ or $\mathbf{k}_2$)

$$\begin{aligned}\mathbf{S} &= \frac{\omega|\Phi|^2}{16\pi k^2}\mathbf{k}\times(\mathbf{k}\times\overline{\overline{\varepsilon}}\cdot\mathbf{k})+cc \\ &= \frac{\omega|\Phi|^2}{16\pi k^2}[\mathbf{k}\,\mathbf{k}\cdot\overline{\overline{\varepsilon}}\cdot\mathbf{k}-\overline{\overline{\varepsilon}}\cdot\mathbf{k}\,k^2]+cc\end{aligned} \tag{21}$$

Using the fact that propagating waves must satisfy the dispersion relation Eq. (14) which is $\mathbf{k}\cdot\overline{\overline{\varepsilon}}\cdot\mathbf{k} = 0$, we are left with just the second term. Furthermore, taking the x-component of **S** leads to an intuitively reasonable result

$$S_x = -\mathrm{Re}\left(\frac{\omega|\Phi|^2}{8\pi}\mathbf{e}_x\overline{\overline{\varepsilon}}\cdot\mathbf{k}\right) = \frac{1}{2}|\Phi|^2\,\mathrm{Re}\,y_w = \frac{1}{2}\mathrm{Re}(\Phi^* J_x) \tag{22}$$

Here Eq. (13) has been used. Comparing with Eq. (21) we see that, as is well known,[30]

$$S_x = v_{gx}\,\mathscr{E} \tag{23}$$

where the energy density of the electrostatic wave is

$$\mathscr{E} = \frac{\omega}{16\pi}\frac{\partial\mathscr{D}}{\partial\omega}|\Phi|^2 = \frac{\omega}{16\pi}\frac{\partial}{\partial\omega}(\mathbf{E}^*\cdot\overline{\overline{\varepsilon}}\cdot\mathbf{E}) \tag{24}$$

The net Poynting flux into the surface (i.e. the difference in the magnitudes of the incoming and reflected Poynting fluxes) gives the power per unit area absorbed by the sheath, P/A_n where A_n is the total surface area of the sheath. Using the normalization of Eq. (2) it follows that

$$P/A_n = S_{x1} + S_{x2} = \frac{1}{2}\mathrm{Re}(y_{w1} + |A|^2 y_{w2}) = \frac{1}{2}\mathrm{Re}(y_{w1})(1-|A|^2) \tag{25}$$

where we have used the fact that for propagating modes, i.e. **k** pure real, $y_{w2} = -y_{w1}^*$. This is proved in Appendix A.

Alternatively, we can evaluate the sheath power dissipation from

$$P_s/A_n = \frac{1}{2}\mathrm{Re}(y_s)|\Phi(0)|^2 = \frac{1}{2}\mathrm{Re}(y_s)|1+A|^2 \tag{26}$$

This manuscript was accepted by Phys. Plasmas. Click here to see the version of record.

where $V_s = \Phi(0) = 1+A$ is the RF sheath voltage and $y_s = 1/z_s$. It is shown in Appendix B that energy is conserved, i.e. $P = P_s$. As a result, the fraction of the incident power that is absorbed is

$$f_P = 1 - |A|^2 \tag{27}$$

Unfortunately a general calculation of power transfer for evanescent modes is not presently available. However, for the special case of perpendicular incidence, an illustration of power transfer between two overlapping evanescent modes and a corresponding analytic proof of energy conservation is given in Appendix C. The general case is treated numerically in the following.

B. Sample results

Figure 3 illustrates a sample solution for the behavior of the SW vs. density. For the chosen parameters (see caption) there is a lower hybrid (LH) resonance ($\varepsilon_\perp = 0$) at $n_e = n_{eLH} = 3.16\times10^{10}$ cm^{-3} ($\log_{10} n_e/\text{cm}^3 = 10.5$). Below this density the SW is propagating, but both values of k_x that satisfy the dispersion relation are negative due to the SW behavior at oblique angles of propagation. However the group velocity indicates distinct incoming and outgoing branches. For $n_e > n_{eLH}$ the SW is evanescent and the incoming branch is the one with Im $k_x > 0$. These choices allow identification of k_{x1} and k_{x2} for use in evaluating ρ_1 and ρ_2 required in Eq. (7).

The parameters chosen in Fig. 3 to compute ρ_j are for large k_t and large ξ. Large k_t is chosen to insure validity of the electrostatic approximation, viz. $n_\perp^2 >> \varepsilon_{||}$. This choice is consistent with pure slow wave propagation but has other consequences as well, as discussed in Sec. VI. Large k_t and ξ tend to make $|\rho_j| > 1$ almost everywhere in the plot because y_w scales with k, and large ξ results in large z_s. However, even in this case, $|\rho_j|$ becomes small near the LH resonance. The reason is evident from Eq. (13). The first term in y_w is negligible when $\varepsilon_\perp$ is nearly zero. The second term is usually dominant because of the large $\varepsilon_{||}$ factor; however, when $\varepsilon_\perp = 0$ and $k_\perp$ is finite then $k_{||} = 0$ from the dispersion relation which eliminates the second term. Finally, the third term, proportional to $b_y k_z$, remains non-zero, but is numerically small.

Finally, note that in the electrostatic approximation, a solution of the dispersion relation remains a solution when **k** is multiplied by a constant. Since y_w is directly proportional to the magnitude of **k**, this means that ρ_j in Fig. 3(c) also scales with the magnitude of **k**. At small k, and hence small ρ_j we might expect more of the domain to be in the intermediate $|\rho_j| \sim 1$ or quasi-conducting $|\rho_j| < 1$ limits. These points and the role of electromagnetic effects, important at small k, are addressed in Sec VII.

This manuscript was accepted by Phys. Plasmas. Click here to see the version of record.

IV. Variation of |A| with parameters

Following the method outlined in Sec. III, for given parameters the dispersion relation may be used to obtain k_x for the incoming and outgoing waves (distinguished by the sign of Im k_x and v_{gx}). This allows the calculation of ρ_1, ρ_2 and finally A, the relative amplitude of the outgoing wave. In this section we discuss the variation of |A| with density, magnetic field angle with respect to the surface, wave-vector, frequency and magnetic field strength. Attention is restricted to a fixed value of RF wave amplitude, $\xi = 20$ unless otherwise noted because high voltage RF sheaths are the main ones of practical interest. However, it should be kept in mind that while the fixed ξ analysis presented here can be useful for intuition, it is not the whole story: where the amplification factor |A| is large, ξ will increase, and this can change z_s, hence ρ and A itself. Nonlinear feedback of this sort can be important near the sheath-plasma resonance. This point is discussed in Sec. V when we compare results with the rfSOL code; it has also been treated in a separate more detailed investigation.[28]

A. Variation with density and magnetic field angle

Figure 4 shows an example of the variation of |A| in the (n_e,φ) plane. Other parameters are given in the caption. In the low density regime, $n_e < n_{eLH}$ where the SW is propagating, contours are labeled by the power absorption percentage f_p defined by Eq. (27). Near n_{eLH} most of the incoming power is absorbed by the sheath while at lower densities the power absorption fraction gradually declines. In the model investigated here, there is a modest dependence on the magnetic field angle over the range considered, some of which arises from the sheath impedance z_s and some from k_x through the wave propagation properties. In the high density regime $n_e > n_{eLH}$ where the SW is evanescent, contours in Fig. 4 are labelled by |A|. Substantial amplification occurs near n_{eLH} particularly for grazing incidence magnetic field lines (small φ). At high densities |A| gradually falls off to near unity values. These features are also seen in Fig. 5 which shows a cut along $\varphi = 0.15$ radians to illustrate the structure of |A| near the LH resonance and over a larger range of densities.

The reason for the strong variation across the LH resonance is the same as given in Sec. III. The quantities ρ_j are proportional to y_{wj} and y_{wj} depends sensitively on density directly through $\varepsilon_\perp$ and indirectly through $k_{||j}$ and the dispersion relation. The fact that $|\rho_j|$ is typically large for the illustrated wavenumbers, and the reduction of $|\rho_j|$ as LH resonance is approached means that there is always some density near the LH resonant density such that $|\rho_j| \sim 1$. The variation is strongest at glancing oblique angles because of the properties of z_s: the electron sheath admittance is reduced at glancing angles because of the smaller geometrical projection of electron parallel current normal to the wall.[22] This tends to make the total sheath impedance less resistive and more capacitive allowing for a strong sheath-plasma resonance, $\rho_2 \sim 1$, near n_{eLH}.

B. Variation with k_y

For the base case parameters B = 2 T, $\omega = 2\Omega_i$, T_e = 15 eV, k_z = 1.6/cm, ξ = 20, the variation of f_p and |A| for vs. k_y is shown in Fig. 6. Instead of showing multiple contour plots of the form of Fig. 4, here we show the maximum (solid line) and average (dashed line) values of f_p and |A| over the range $n_e = 10^{10}$ to $10^{12.5}$ cm^{-3} and φ over the range 0.1 to $\pi/2$. The density and angle at which the maximum values occur are given in the lower panels and remain within the scanned ranges. In particular, as expected for these parameters, the maximizing density is near n_{eLH} occurring ever closer as k_y increases in order to compensate for the explicit k dependence of y_{wj} and allow $\rho_2 \sim 1$. The angle for maximum power absorption does show variation with k_y, but the maximum is rather broad in φ (see Fig. 4) so not much significance should be placed on this. (Because the "ridge" or maximum contour of f_p is nearly independent of φ over a range, the actual φ location of the maximum is not well defined.) The base case shown in Fig. 4 with k_y = 0.2 /cm is seen to be reasonably typical: over a large range of k_y, we find f_p as large as 80% and |A| exceeding 6 near n_{eLH} and at small φ. There is little change in any of the plots in Fig. 6 for k_y < 0.05 /cm, which is effectively the $k_y \rightarrow 0$ limit. Note that k_z remains fixed at 1.6/cm for the scan.

C. Variation with magnetic field strength and RF frequency

In order to facilitate application to experiments and modeling, the scans in this paper are mostly shown in dimensional units. However, one important dimensionless invariant parameter combination exists. If the magnetic field strength, B, is changed at constant ω/Ω_i then the results remain invariant if density is scaled by B^2. More explicitly, if λ is a scaling parameter, then the following is an invariant transformation: $B \rightarrow \lambda B$, $\omega \rightarrow \lambda\omega$, $n_e \rightarrow \lambda^2 n_e$, $\mathbf{k} \rightarrow \lambda\mathbf{k}$, $T_e \rightarrow T_e$, $V_{rf} \rightarrow V_{rf}$, $\varphi \rightarrow \varphi$. These fundamental transformation rules imply $\Omega \rightarrow \lambda\Omega$, $\hat{\omega} \rightarrow \hat{\omega}$, $\hat{\Omega} \rightarrow \hat{\Omega}$, $\hat{z} \rightarrow \hat{z}$, $\varepsilon \rightarrow \varepsilon$, $y_w \rightarrow \lambda^2 y_w$, $z_s \sim \lambda_d/\omega_{pi} \sim 1/n_e \rightarrow z_s/\lambda^2$, $\rho \sim y_w z_s \rightarrow \rho$. Thus ρ and therefore A are invariant under this transformation. Consequently, it will not be necessary to explore the dependence of A on the magnetic field strength at fixed ω/Ω_i.

We have seen that for our base case parameters $|\rho_j| > 1$ pertains except near LH resonance. However, not all parameter choices lead to $|\rho_j| > 1$ even if k_z is chosen to be relatively large, as it is for our base case. A high harmonic fast wave (HHFW) case is shown in Fig. 7. Parameters are the same as the base case except that $\omega = 20\ \Omega_i$ and the line plot in Fig. 7 is for φ = 0.4, k_y = 0.2/cm. In this case because the dielectric tensor, hence y_{wj}, scales inversely with ω^2 in the HHFW limit, the resulting values of ρ_j are order unity or smaller. Other cases that do not result in the quasi-insulating limit will be discussed in the section summary, Sec. IV D.

This manuscript was accepted by Phys. Plasmas. Click here to see the version of record.

Similar to Fig. 6, Fig. 8 illustrates the maximum values of f_p and $|A|$ in the (n_e,φ) plane for a given value of k_y. Expect for $\hat{\omega}$, parameters are the same as the base case parameters employed in Fig. 6. In addition to the results for the base case, and for the HHFW case just discussed, Fig. 8 shows results for a case just above cyclotron resonance ($\hat{\omega} = 1.05$), and a case below cyclotron resonance ($\hat{\omega} = 0.5$). Qualitatively similar cases can occur in tokamak scenarios with multiple species, and/or on wall locations other than at the low field side. In these cases $|\rho_j|$ tends to be large because both the dielectric tensor and k are large and either the LH resonance is outside the scanned range of n_e ($\hat{\omega} = 1.05$) or is not present at all ($\hat{\omega} = 0.5$). Then impedance matching cannot occur. Consequently, f_p drops to a small value, and $|A|$ is near unity: the wave reflects from the sheath with little absorption or amplification.

D. Summary of dependence on parameters

In this section we have seen that $|A|$, which is controlled by $|\rho_j|$, can depart significantly from unity under some conditions, leading to large power absorption fractions (propagating wave case) or large surface wave amplification (evanescent wave case). These situations occur, according to Eq. (7), when $|\rho_j| \sim 1$.

For base case ICRF parameters and large k (to justify an electrostatic analysis) we find that for both incoming and outgoing waves (i.e. $\mathbf{k}_1$ and $\mathbf{k}_2$ resulting in ρ_1 and ρ_2) the impedance ratio is typically large ($|\rho| > 1$) for large sheath voltages ($\xi >> 1$) and densities not close to the LH resonant density. Furthermore, for ω just above but close to cyclotron resonance Ω_i, we find that $|\varepsilon_\perp|$ is large resulting in $|\rho| >> 1$. Also it is typical to have $|\rho| >> 1$ for $\omega < \Omega_i$ at least if $\omega_{pi} > \Omega_i$. On the other hand, since ρ scales with k, the cases $|\rho| \sim 1$ or $|\rho| < 1$ occur when $k_\perp$ is modest or small, (not explicitly considered in this section where electrostatics has been invoked for analytical tractability), when z_s is small (e.g. for lower voltages), or when $\varepsilon_\perp$ is small, which can happen for the HHFW ($\omega >> \omega_{pi}$) case, and near LH resonance ($\varepsilon_\perp = 0$). The variations of ρ and A that come about through the sheath voltage, and at small k including electromagnetic effects, are discussed in the following sections.

V. Comparison with the rfSOL code

The preceding sections of this paper have developed a theory of RF slow wave interaction with a sheath for the idealized case of an incident electrostatic plane wave on a flat surface and a specified RF voltage at the location of the sheath BC. Here in Sec. V, the results of this theory are compared with a much more comprehensive model, the rfSOL code which implements the same sheath BC, Eq. (3), and the same $\hat{z}$ as in the rest of this paper, but in the plasma volume employs: (i) a full wave description with an antenna source that launches a spectrum of modes, (ii) an electromagnetic treatment of both fast and slow RF waves, (iii) a

This manuscript was accepted by Phys. Plasmas. Click here to see the version of record.

shaped wall on which the sheath BC is applied, and (iv) a self-consistent iteration of the sheath voltage with the resulting RF wave fields. The rfSOL code and model geometry for this comparison are discussed in Sec. V A along with the predictions of the theoretical model. In Sec. V B, the rfSOL results are given and compared with the predictions.

A. Geometry and code setup

The rfSOL code is a finite element code that solves the electromagnetic cold fluid RF wave equations in flexible geometry.[25] A sample domain and solution are illustrated in Fig. 9. The RF sheath boundary conditions described in Ref. 22 are implemented on the right hand boundary, which is a wall with a curved surface defined by a Gaussian-shaped "bump." The boundary condition on the left, x = 0, is not relevant here because the waves decay to zero before reaching that boundary. Periodic boundary conditions are invoked at the two ends of the illustrated domain in y. The dark black line at x = 2.26 m is an RF antenna which for the chosen parameters emits evanescent waves in both directions in x (both fast and slow waves, but the fast wave is strongly evanescent for the chosen parameters); the right-going (dominantly slow wave) branch interacts with the wall sheath. In this simulation, the parameters are: $n_e = 1\times10^{18}$ m^{-3}, $B_{0x} = 4$ T, $B_{0y} = B_{0z} = 0$, $k_z = 40$ m^{-1}, $\omega/2\pi = 80$ MHz, $T_e = 15$ eV and the maximum antenna current is $K_{max} = 12$ kA/m. This relatively high density case results in the evanescent SW illustrated in the figure. Note that for these parameters, the lower hybrid resonant density is $n_{eLH} = 2.48\times10^{17}$ m^{-3} which is well below the density employed.

The predictions of the electrostatic analysis for ρ, while not fully justified for these parameters, prove useful for understanding, and are shown in Fig. 10 as a function of the dimensionless RF voltage parameter ξ for three values of k_z. The two sets of lines for each case are for the incoming and outgoing branches. For all cases, real and imaginary parts start out with magnitudes less than one and increase in magnitude monotonically as ξ is increased. Note that ρ_j is roughly proportional to k_z as expected from the proportionality of y_{wj} with $\mathbf{k}_j$. The values of ξ where Re $\rho_2 \approx 1$ are of significance for strong wave amplification, i.e. sheath-plasma wave resonance; see Eq. (7). This occurs at $\xi \sim 8$ for $k_z = 160$/m, $\xi \sim 16$ for $k_z = 80$/m and $\xi \sim 32$ for $k_z = 40$/m. Note also that for the $k_z = 40$/m case, at Re $\rho_2 = 1$ we find Im $\rho_2 <$ Re ρ_2, whereas the real and imaginary parts are similar at Re $\rho_2 = 1$ for $k_z = 160$ /m. These points will be important in interpreting the rfSOL results that follow.

B. Results from rfSOL

Because the rfSOL results reported here were obtained for a constant density and magnetic field throughout the domain, the waves in the plasma volume are described by the usual cold plasma dispersion relation. In the electrostatic limit, this is just Eq. (14). Our previous

published work[25] has verified the rfSOL solutions for various constant density cases. The main point of interest here is in understanding the interaction of the waves with the sheath boundary condition in rfSOL using the wave-sheath impedance model as exemplified in Fig. 10. It is shown that the rfSOL results can be qualitatively understood by examining the value of ρ, i.e. the ratio of the sheath and wave impedances.

The plasma-sheath interaction for the same parameters used in Figs. 9 and 10 is shown for the two k_z values, 160 m^{-1} and 40 m^{-1} in the left and right panels respectively of Fig. 11. As the antenna current $\propto K_{max}$ is increased for a given k_z, it drives proportional amounts of plasma current, thus D_n/K_{max} is roughly independent of K_{max} (lowest panels). From the sheath BC this means that V_{rf}/K_{max} is roughly proportional to z_s for fixed k_z (upper and middle panels). Note also that since $D_n \sim \mathbf{s}\cdot\bar{\bar{\varepsilon}}\cdot\mathbf{E} \sim b_n\varepsilon_{||}E_{||}$ and the surface function b_n and $\bar{\bar{\varepsilon}}$ are not varied in this K_{max} scan, $E_{||}/K_{max}$ will also be roughly independent of K_{max} (verified but not shown).

At low voltages (either low peak voltage or at spatial locations away from the large RF fields) $|V_{rf}|/K_{max}$ is independent of K_{max} (upper panels) indicating a linear sheath response. At high voltages the sheath is nonlinear.

The maximum values of normalized sheath voltage ξ_{max} for a K_{max} scan are summarized in Fig. 12 for k_z = 40, 80 and 160 m^{-1}. From Fig. 10 we see that as ξ increases, $|\rho|$ also increases, passing through $|\rho| \sim 1$ for some value of $\xi \equiv \xi_1(k_z)$ that increases as k_z decreases. For $\xi \sim \xi_1$ a sheath-plasma wave (SPW) resonance is possible, according to Eq. (7), if Re $\rho_2 \approx 1$ and Im ρ_2 < Re ρ_2. This occurs most dramatically for the k_z = 40 m^{-1} case where $|\rho| \sim 1$ is also maintained for a larger range of ξ than in the larger k_z cases. This accounts for the rapid growth in Fig. 12 of $|V_{rf}|$ between K_{max} = 4 and 5 kA/m for k_z = 40 m^{-1}: as $|V_{rf}|$ increases, $|z_s|$ also increases. When it increases enough to make $|\rho| \sim 1$ then A becomes large, and hence the self-consistent value of $|V_{rf}|$ is also large. For very large ξ, $|\rho| >> 1$ eventually pertains and the $\xi_{max}(K_{max})$ curves pass through resonance and again have smaller slopes.

The arrows in Fig. 12 indicate the approximate location of the steepest slope parts of each curve; these conditions may be identified with the SPW resonance. For larger values of k_z, the SPW resonance shifts to smaller ξ in qualitative agreement with Fig. 10, and the resonant behavior in Fig. 12 is eventually almost lost for k_z = 160 m^{-1} where Fig. 10 indicates a substantial Im ρ_2 when Re $\rho_2 \approx 1$.

While the theoretical model captures some important qualitative features of these rfSOL code runs, there are some quantitative differences. In the rfSOL code, the sheath-plasma resonance is also observed for k_z = 80 m^{-1}, but not for k_z = 160 m^{-1} even though Im ρ_2 is similar to Re ρ_2 for those cases, according to Fig. 10. Also the theoretical approach predicts strong wave amplification at $\xi \approx 8$, 16, and 32 for k_z = 160, 80, and 40 m^{-1}, respectively, while the rfSOL code gives the largest slopes at $\xi \approx 8$, 27, 44 for the same respective k_z values. The additional

This manuscript was accepted by Phys. Plasmas. Click here to see the version of record.

physics in the rfSOL code beyond that in the theoretical mode, as discussed at the beginning of Sec. V, are likely reasons for these quantitative differences.

These rfSOL results depend on (i) employing a nonlinear z_s model that properly accounts for the changes in z_s with sheath voltage, and (ii) a self-consistent solution of the wave properties in the plasma including the nonlinear z_s model. A detailed survey of sheath interactions under the generalized sheath BC for oblique angle sheaths is presented in Ref. 28.

VI. Electromagnetic effects

As shown in Sec. II, the behavior of the RF sheath boundary condition changes from quasi-conducting for $|\rho| << 1$ to quasi-insulating for $|\rho| >> 1$ with sheath-plasma wave resonance possible in the intermediate case where $\rho_2 \approx 1$. Also, as mentioned previously, in the electrostatic model, y_w and hence ρ are proportional to the wave-vector $\mathbf{k}$. Thus as $\mathbf{k}$ is varied from small to large, a full range of regimes is encountered. In practical applications, note that $\mathbf{k}$ is determined both by the spectrum launched by the antenna and by the scale of surface objects that the waves encounter at the boundary.

However, the situation described in the previous paragraph is not entirely correct because the electrostatic model is not valid at small k: the typical electrostatic validity condition for the SW is $n_\perp^2 > \varepsilon_{||}$. To test the qualitative accuracy of the present electrostatic theory in low k situations, electrostatic and electromagnetic results are compared in this section.

Unfortunately a semi-analytic electromagnetic theory analogous to the electrostatic theory of Sec. II does not appear to be tractable. Not only does the scalar electrostatic impedance generalize to a 2×2 impedance matrix, coupling fast and slow waves, but also the general fourth order dispersion relation for obliquely propagating fast and slow waves is not analytically soluble. Such a 2×2 impedance matrix would be closely related to the calculation of connection coefficients for fast and slow waves.[16] Here we adopt a more modest goal: comparison of electrostatic and electromagnetic results for the slow wave alone. For the preceding reasons, a fully numerical approach is taken here. The method is summarized in Appendix D.

Electrostatic and electromagnetic results are compared in Fig. 13 for a range of values of $\mathbf{k}_t$. Other parameters are: B = 2 T, $\xi = 20$, $\omega = 2\,\Omega_i$, $n_e = 10^{10}$ cm^{-3}, $\varphi = \pi/2$ and the plasma ions are deuterium. The usually quoted condition for validity of the electrostatic approximation for the slow wave is $\varepsilon_{||}/n_\perp^2 << 1$. For these parameters, this implies the condition $k_\perp = (k_y^2+k_z^2)^{1/2} >> 0.19$ /cm. When $k_z = 1.6$ cm^{-1}, as for most of the examples in this paper, the electrostatic and electromagnetic results are, not surprisingly, essentially indistinguishable. As k_z is reduced noticeable differences are seen. However, although the electrostatic model is not strictly valid for $\mathbf{k}_t \to 0$, it captures the qualitative trends for all $\mathbf{k}_t$, even those with magnitudes comparable to and

This manuscript was accepted by Phys. Plasmas. Click here to see the version of record.

below 0.19/cm. In particular, for small $\mathbf{k}_t$ the sheath becomes conducting ($A \to -1$) while for large $\mathbf{k}_t$ it is quasi-insulating ($A \to 1$) in both the electrostatic and fully electromagnetic models.

Finally, it should be noted that the electrostatic approximation not only introduces quantitative changes in the slow wave interaction with the sheath, it also eliminates the possibility of slow-to-fast wave mode conversion. This effect is included in calculating the electromagnetic results for Fig. 13, and appears not to be qualitatively important, at least for the illustrated parameters. (The process of fast-to-slow wave mode conversion by sheath interaction is another matter, and is often quite important,[10,16,19,27] but is outside the scope of this paper.)

VII. Summary and conclusions

In this paper we have studied the interaction of electrostatic RF slow waves with an RF sheath that is described by an effective surface impedance implemented as a sheath boundary condition. The interaction is controlled by the ratio of wave impedance to sheath impedance, defined by Eq. (8) through the quantity ρ_j. Limiting asymptotic cases of small and large $|\rho_j|$ correspond to quasi-conducting and quasi-insulating sheaths.

In general, an incident or incoming wave is both reflected and absorbed by the sheath. The amplitude A of the reflected wave is given in terms of ρ_j ($j = 1,2$), by Eq. (7), which depends on the incident and reflected wave impedances. Once A has been calculated the fraction of incident power absorbed in the sheath can be calculated for propagating waves using Eq. (27). For evanescent waves, which occur for densities above the lower hybrid resonant density, i.e. when $\varepsilon_\perp > 0$, the amplitude $|A|$ can be larger than unity, indicating amplification of the evanescent reflected (outgoing) wave. Depending on plasma and wave parameters, the condition $\rho_2 \approx 1$ may be approximately met, in which case $|A| >> 1$ occurs, a result which indicates a sheath-plasma wave resonance.

The variations of A with plasma density, magnetic field angle, RF wave-vector and frequency, have been explored: the main findings are summarized in Sec. IV. D. A case resulting in sheath-plasma wave resonance was presented in Sec. V, where the predictions of the semi-analytical theory of the previous sections were compared with and used to understand results from the rfSOL code. Finally it was shown that the electrostatic theory of this paper captures the qualitative trends of a fully electromagnetic treatment at least for a low density, perpendicular ($|b_n| = 1$) sheath.

Several potentially useful generalizations of the present work are apparent. As already discussed, a fully electromagnetic treatment accounting directly for the fast wave and possible sheath-mediated mode-conversions between fast and slow waves would be ideal. In this respect, it would be most useful to have a semi-analytical approach, along the lines of the present paper,

in order to gain insight and enable *a priori* estimation and understanding of different sheath interaction regimes.

Another useful generalization would be to consider multiple ion species, since more than one species is often present in ICRF scenarios, deliberately and additionally through unwanted edge impurities. The theoretical development of this paper remains valid in this case; one would only have to employ multi-ion species forms of the dielectric tensor and the sheath impedance. While the former is easily done, a multi-ion species generalization of the sheath impedance parametrization, i.e. $\hat{z}(\hat{\omega},\hat{\Omega},b_n,\xi)$ is not presently available.

Simulations that self-consistently solve for the RF fields driven by an antenna in the presence of surface sheaths are needed to provide a complete description of RF interactions at the plasma-material interface. The magnitude of the resulting sheath potential and surface power deposition depend on the regime of RF-sheath interaction. The identification of an appropriate wave impedance, and a corresponding dimensionless parameter controlling these interactions is the main contribution of the present paper. It is hoped that the regime and parameter analysis provided herein may be beneficial in understanding the results emerging from ongoing RF simulations and experiments on RF boundary plasma interactions.

Acknowledgements

This material is based upon work supported by the U.S. Department of Energy Office of Science, Office of Fusion Energy Sciences under Award Numbers DE-AC05-00OR22725 sub-contract 4000158507 and DE-FG02-97ER54392; and under JSPS KAKENHI Grant Number JP16K18336. Discussions with team members of the RF SciDAC project (Discovery through Advanced Computing Initiative: Center for Integrated Simulation of Fusion Relevant RF Actuators) are gratefully acknowledged. This research used resources of the National Energy Research Scientific Computing Center, a DOE Office of Science User Facility supported by the Office of Science of the U.S. Department of Energy under Contract No. DE-AC02-05CH11231.

Appendix A: Incident and reflected wave admittance

This appendix establishes the relationship between y_{w1} and y_{w2} where indices 1 and 2 enumerate the two roots of the SW dispersion relation. In general y_w is defined by Eqs. (9) or (13) repeated here

$$y_w = -\frac{\omega}{4\pi}\mathbf{e}_x\cdot\bar{\bar{\varepsilon}}\cdot\mathbf{k} = -\frac{\omega}{4\pi}[\varepsilon_\perp k_x + (\varepsilon_{||}-\varepsilon_\perp)b_x k_{||} + i\varepsilon_\times \mathbf{e}_x\cdot\mathbf{b}\times\mathbf{k}] \qquad (A1)$$

We will first show that $\mathrm{Re}\,\mathbf{e}_x\cdot\bar{\bar{\varepsilon}}\cdot(\mathbf{k}_1+\mathbf{k}_2)=0$, i.e. that $\mathrm{Re}\,y_{w1} = \mathrm{Re}\,y_{w2}$. It is assumed throughout this appendix that $\mathbf{k}$ is pure real, i.e. the modes are freely propagating. This is the

This manuscript was accepted by Phys. Plasmas. Click here to see the version of record.

only situation in which the final result Eq. (A10) is needed, for use in the main text in Eq. (25), i.e. for propagating, not evanescent modes.

$$\mathrm{Re}\ \mathbf{e}_x \cdot \bar{\bar{\varepsilon}} \cdot (\mathbf{k}_1 + \mathbf{k}_2) = \varepsilon_\perp (k_{x1} + k_{x2}) + (\varepsilon_\parallel - \varepsilon_\perp) b_x (k_{\parallel,1} + k_{\parallel,2}) \tag{A2}$$

Substituting for $k_\parallel = b_x k_x + \mathbf{b}_t \cdot \mathbf{k}_t$ for $k_{\parallel,1}$ and $k_{\parallel,2}$ where t represents the tangential (y and z) components which are identical for $\mathbf{k}_1$ and $\mathbf{k}_2$ one obtains

$$\mathrm{Re}\ \mathbf{e}_x \cdot \bar{\bar{\varepsilon}} \cdot (\mathbf{k}_1 + \mathbf{k}_2) = (k_{x1} + k_{x2})[\varepsilon_\perp + (\varepsilon_\parallel - \varepsilon_\perp) b_x^2] + 2(\varepsilon_\parallel - \varepsilon_\perp) b_x \mathbf{b}_t \cdot \mathbf{k}_t \tag{A3}$$

The dispersion relation, Eq. (14) may be written as $k^2 \varepsilon_\perp + (\varepsilon_\parallel - \varepsilon_\perp) k_\parallel^2 = 0$ or

$$(k_x^2 + k_t^2)\varepsilon_\perp + (\varepsilon_\parallel - \varepsilon_\perp)(b_x k_x + \mathbf{b}_t \cdot \mathbf{k}_t)^2 = 0 \tag{A4}$$

Expanding, collecting powers of k_x and dividing through to make the coefficient of k_x^2 unity yields

$$k_x^2 + \frac{2k_x(\varepsilon_\parallel - \varepsilon_\perp) b_x \mathbf{b}_t \cdot \mathbf{k}_t}{\varepsilon_\perp + (\varepsilon_\parallel - \varepsilon_\perp) b_x^2} + \frac{k_t^2 \varepsilon_\perp + (\varepsilon_\parallel - \varepsilon_\perp)(\mathbf{b}_t \cdot \mathbf{k}_t)^2}{\varepsilon_\perp + (\varepsilon_\parallel - \varepsilon_\perp) b_x^2} = 0 \tag{A5}$$

But we also know, by definition, that the roots of this equation are k_{x1} and k_{x2} hence

$$\begin{aligned} (k_x - k_{x1})(k_x - k_{x2}) &= 0 \\ k_x^2 - k_x(k_{x1} + k_{x2}) + k_{x1} k_{x2} &= 0 \end{aligned} \tag{A6}$$

Comparing coefficients of the powers of k_x in Eqs. (A5) and (A6) we have

$$\begin{aligned} k_{x1} + k_{x2} &= -\frac{2(\varepsilon_\parallel - \varepsilon_\perp) b_x \mathbf{b}_t \cdot \mathbf{k}_t}{\varepsilon_\perp + (\varepsilon_\parallel - \varepsilon_\perp) b_x^2} \\ k_{x1} k_{x2} &= \frac{k_t^2 \varepsilon_\perp + (\varepsilon_\parallel - \varepsilon_\perp)(\mathbf{b}_t \cdot \mathbf{k}_t)^2}{\varepsilon_\perp + (\varepsilon_\parallel - \varepsilon_\perp) b_x^2} \end{aligned} \tag{A7}$$

The result for $k_{x1} + k_{x2}$ is exactly what is needed in Eq. (A3) and yields

$$\mathrm{Re}\ \mathbf{e}_x \cdot \bar{\bar{\varepsilon}} \cdot (\mathbf{k}_1 + \mathbf{k}_2) = 0 \tag{A8}$$

On the other hand, the imaginary parts of y_w are trivially related

$$\mathrm{Im}\ \mathbf{e}_x \cdot \bar{\bar{\varepsilon}} \cdot \mathbf{k} = \varepsilon_\times \mathbf{e}_x \cdot \mathbf{b} \times \mathbf{k} = \varepsilon_\times \mathbf{e}_x \cdot \mathbf{b} \times \mathbf{k}_t \tag{A9}$$

This relationship is independent of k_x and hence the same for $\mathbf{k}_1$ and $\mathbf{k}_2$. Thus we have from Eq. (A8), Re y_{w2} = –Re y_{w1}, and from Eq. (A9), Im y_{w2} = Im y_{w1} or equivalently

$$y_{w2} = -y_{w1}^{*} \tag{A10}$$

Appendix B: Power balance

In this Appendix, we prove the equivalence of Eqs. (25) and (26), i.e. that

$$\mathrm{Re}(y_{w1})(1-|A|^2) = \mathrm{Re}(y_s)|1+A|^2 \tag{B1}$$

The proof is straightforward using Eqs. (7) , (8) and (A10)

$$A = -\frac{y_{w1}/y_s - 1}{y_{w2}/y_s - 1} = \frac{y_{w1} - y_s}{y_{w1}^{*} + y_s} \tag{B2}$$

An explicit result for y_{w1} is not needed. It is sufficient to employ

$$\begin{aligned} y_{w1} &= y_{w1r} + i y_{w1i} \\ y_s &= y_{sr} + i y_{si} \end{aligned} \tag{B3}$$

Substituting Eq. (B3) into the final form for A in Eq. (B2), it follows, after straightforward algebraic manipulations, that the left and right hand sides of Eq. (B1) are indeed equal.

Appendix C: Poynting flux and power transfer of overlapping evanescent modes

It is well known that a single evanescent mode cannot carry any net Poynting flux. However, it is possible for two overlapping evanescent modes to transfer energy between them. In the evanescent slow wave examples of this paper the mode which decays towards the sheath in Fig. 1 can transfer energy to the evanescent mode that maximizes on the sheath surface and decays into the plasma volume. In fact, this is the mechanism that enables RF power loss to the sheath and also enables amplification of the latter mode by the sheath-plasma resonance.

A simple example of energy transfer between evanescent modes is illustrated in the present appendix. We consider perpendicular incidence ($\varphi = \pi/2$), $k_y = 0$, $\mathbf{k}_t = k_z\mathbf{e}_z$ and hence $E_y = 0$ in the electrostatic limit. From the dispersion relation for slow waves we find that $k_{2x} = -k_{1x} \equiv -k_x$ and hence $k_1^2 = k_2^2 \equiv k^2$. These assumptions greatly simplify the algebra.

At the location of the sheath, from Eq. (5),

$$\mathbf{E} = -ik_x(1-A)\mathbf{e}_x - ik_z(1+A)\mathbf{e}_z \tag{C1}$$

This manuscript was accepted by Phys. Plasmas. Click here to see the version of record.

From Eq. (20), for a single plane wave ~ $\exp(ik_x x+ik_z z)$,

$$B_{1y} = \frac{1}{n^2}(n_z D_x - n_x D_z) \tag{C2}$$

where in the present geometry with $\mathbf{b} = \mathbf{e}_x$ we have for the incoming wave given by the first term in Eq. (2): $D_x = \mathbf{e}_x \cdot \bar{\bar{\varepsilon}} \cdot \mathbf{E} = -i\varepsilon_{||} k_x$ and $D_z = \mathbf{e}_z \cdot \bar{\bar{\varepsilon}} \cdot \mathbf{E} = -i\varepsilon_{\perp} k_z$. The D_x term dominates because of the $\varepsilon_{||}$ factor. When multiple waves are present care must be taken because the incoming and outgoing waves have opposite signs of k_x. This accounts for the change in the sign of the A term in the x-component of Eq. (C1). Thus taking into account both waves and dropping the D_z term

$$B_{1y} \approx -\frac{i\omega}{c}\frac{k_x k_z}{k^2}\varepsilon_{||}(1-A) \tag{C3}$$

Using $E_z^* = ik_z(1+A^*)$ and substituting it and Eq. (C3) into the definition of the Poynting flux given by Eq. (19) yields

$$S_x = -\frac{\omega}{16\pi}(1+A^*)(1-A)k_x\varepsilon_{||} + cc \tag{C4}$$

where we approximate $k^2 \approx k_{\perp}^2 = k_z^2$ using the slow wave ordering . In the following we will use the identity

$$(1+A^*)(1-A) = 1-|A|^2 - 2iA_i \tag{C5}$$

where A_i = Im A.

For propagating waves the k vector is pure real and Eq. (C4) becomes

$$S_x = -\frac{\omega}{8\pi}(1-|A|^2)k_x\varepsilon_{||} \tag{C6}$$

The wave admittance for the geometry considered here is, from Eq. (13),

$$y_w = -\frac{\omega}{4\pi}k_x\varepsilon_{||} \tag{C7}$$

which is pure real, thus we recover Eq. (25) of the main text

$$S_x = \frac{1}{2}(1-|A|^2)\,\mathrm{Re}\,y_w \tag{C8}$$

On the other hand, for evanescent waves k_x is pure imaginary, and we take

$$k_x = i\kappa \tag{C9}$$

where $\kappa > 0$ gives the correct branch for the incoming wave. In this case the surviving term comes from $2iA_i$, which physically represents the cross term or power transfer between incoming and outgoing branches. Thus the power per unit area transferred between the evanescent waves is

$$P/A_n = S_x = -\frac{\omega}{4\pi} A_i \kappa \varepsilon_{||} = A_i \, \mathrm{Im}\, y_w \tag{C10}$$

This can be considered as a type of evanescent tunneling. Of course, if just the incoming wave were present, i.e. $A \to 0$, then $S_x = 0$ as expected.

Power balance may also be proved in this case. For evanescent waves in this example, we have, from Eqs. (7) and (8), noting that $\rho_2 = -\rho_1$,

$$A = \frac{iy_{wi} - y_s}{iy_{wi} + y_s} \tag{C11}$$

The sheath power dissipation is still given by Eq. (26). We expect that the power transferred from the incoming wave is dissipated in the sheath. This occurs if

$$y_{wi} A_i = \frac{1}{2} y_{sr} |1 + A|^2 \tag{C12}$$

where the definitions in Eq. (B3) are used here also. After some straightforward algebra which does not require explicit results for y_{wi} or y_s it may be shown that Eq. (C12) holds.

Appendix D: Electromagnetic model

In this appendix details of the electromagnetic model employed in Sec. VI are presented. The first step is the numerical solution of Maxwell's equations in the homogenous plasma volume

$$\mathbf{n} \times (\mathbf{n} \times \mathbf{E}) + \bar{\bar{\varepsilon}} \cdot \mathbf{E} = 0 \tag{D1}$$

where $\mathbf{n} = \mathbf{k}c/\omega$ and ω, k_y and k_z are specified. Thus the unknowns are the generalized eigenvalues k_x and the associated eigenvectors $\mathbf{E}$. (Equation (D1) may be rewritten in the form of a generalized eigenvalue problem for k_x by splitting it up into the two constituent Maxwell equations for $\mathbf{E}$ and $\mathbf{B}$. In this appendix, $\mathbf{E}$ and $\mathbf{B}$ will always refer to the RF fields.) The solution provides four normal modes, $\mathbf{k}^{(m)}$ and their associated electric field polarization unit vectors $\mathbf{e}^{(m)}$, m = 1,4. The four modes are the fast and slow waves, each with two directions of propagation (or evanescence). Thus the total electric field is expressed as

$$\mathbf{E} = \sum_m E^{(m)} \mathbf{e}^{(m)} \tag{D2}$$

with as yet undetermined complex amplitudes $E^{(m)}$.

In analogy to the electrostatic procedure, the next step is to specify the incoming wave as a slow wave and solve a set of equations for the outgoing slow and fast waves. The relevant equations are the definitions of the normal components of the current J_n and the RF magnetic field B_n at the sheath interface on the plasma side, and the two tangential components of the sheath BC, Eq. (3):

$$\mathbf{s} \cdot \bar{\bar{\varepsilon}} \cdot \left(\sum_m E^{(m)} \mathbf{e}^{(m)} \right) = \frac{4\pi i}{\omega} J_n \tag{D3}$$

$$-\sum_m E^{(m)} k_n^{(m)} \mathbf{s} \cdot \mathbf{n}^{(m)} \times \mathbf{e}^{(m)} = \mathbf{k}_t \cdot \mathbf{B}_t \tag{D4}$$

$$\left(\sum_m E^{(m)} \mathbf{e}^{(m)} \right) \cdot \mathbf{e}_t = i k_t z_{sh} J_n \tag{D5}$$

$$\left(\sum_m E^{(m)} \mathbf{e}^{(m)} \right) \cdot \mathbf{e}_z = i k_z z_{sh} J_n \tag{D6}$$

Here, recall that **s** is the unit normal pointing from the surface into the plasma so that $J_n = \mathbf{J} \cdot \mathbf{s}$. (We do not use **n** for the unit normal to avoid confusion with the index of refraction, but retain the notations n and t as subscripts denoting normal and tangential.) Equation (D4) is obtained from $\mathbf{n} \times \mathbf{E} = \mathbf{B}$ by dotting with **s**, multiplying by k_n and using $k_n B_n = -\mathbf{k}_t \cdot \mathbf{B}_t$. This manipulation is employed for numerical reasons but also possess an aesthetically pleasing symmetry: $J_n \propto \mathbf{s} \cdot \mathbf{k}_t \times \mathbf{B}_t$ is one "source" term, while the complementary quantity $\mathbf{k}_t \cdot \mathbf{B}_t$ is the other.

Suppose we label the incoming fast and slow waves as $E^{(1)}$ and $E^{(2)}$ respectively, where in the present application $E^{(1)} = 0$ and $E^{(2)} = 1$. Then Eqs. (D3) – (D5) are solved for J_n, $\mathbf{k}_t \cdot \mathbf{B}_t$, $E^{(3)}$ and $E^{(4)}$ where $E^{(3)}$ and $E^{(4)}$ are the outgoing fast and slow waves, respectively. The electromagnetic result plotted in Fig. 13 is obtained as

$$A = \frac{E^{(4)} e_z^{(4)}}{E^{(2)} e_z^{(2)}} \tag{D7}$$

analogous to the ratio of outgoing to incoming electrostatic potentials for the slow wave defined by the amplitude A in Eq. (2).

References

[1] J.-M. Noterdaeme and G. Van Oost, Plasma Phys. Control. Fusion **35,** 1481 (1993).

[2] J.R. Myra, D.A. D'Ippolito, D.A. Russell, L.A. Berry, E.F. Jaeger and M.D. Carter, Nucl. Fusion **46** S455 (2006).

[3] S. J. Wukitch, M. L. Garrett, R. Ochoukov, J. L. Terry, A. Hubbard, B. Labombard, C. Lau, Y. Lin, B. Lipschultz, D. Miller, M. L. Reinke, D. Whyte, and Alcator C-Mod Team, Phys. Plasmas **20**, 056117 (2013).

[4] V. Bobkov, M. Balden, R. Bilato, F. Braun, R. Dux, A. Herrmann, H. Faugel, H. Fünfgelder, L. Giannone, A. Kallenbach, H. Maier, H.W. Müller, R. Neu, J.-M. Noterdaeme, Th. Pütterich, V. Rohde, N. Tsujii, F. Zeus, H. Zohm and the ASDEX Upgrade Team, Nucl. Fusion **53**, 093018 (2013).

[5] J. Jacquot, D. Milanesio, L. Colas, Y. Corre, M. Goniche, J. Gunn, S. Heuraux, and M. Kubi, Phys. Plasmas **21**, 061509 (2014).

[6] C. M. Qin, Y. P. Zhao, H. Q. Wang, X. J. Zhang, B. N. Wan, J.-M. Noterdaeme, F. Braun, V. Bobkov, H. Kasahara, E. H. Kong, L. Wang, Y. Shuai, Z. X. He, B. J. Ding, ICRF Team and EAST Team, Plasma Phys. Control. Fusion **55**, 015004 (2013).

[7] Y. Corre, M. Firdaouss, L. Colas, A. Argouarch, D. Guilhem, J. Gunn, C Hamlyn-Harris, J. Jacquot, M. Kubic, X. Litaudon, M. Missirlian, M. Richou, G. Ritz, D. Serret and K. Vulliez, Nucl. Fusion **52**, 103010 (2012).

[8] I. Cziegler, J. L. Terry, S. J. Wukitch, M. L. Garrett, C. Lau and Y. Lin, Plasma Phys. Control. Fusion **54**, 105019 (2012).

[9] R.J. Perkins, J.-W. Ahn, R.E. Bell, A. Diallo, S. Gerhardt, T.K. Gray, D.L. Green, E.F. Jaeger, J.C. Hosea, M.A. Jaworski, B.P. LeBlanc, G.J. Kramer, A. McLean, R. Maingi, C.K. Phillips, M. Podesta, L. Roquemore, P.M. Ryan, S. Sabbagh, F. Scotti, G. Taylor and J.R. Wilson, Nucl. Fusion **53**, 083025 (2013).

[10] R. Ochoukov, D. G. Whyte, D. Brunner, D. A. D'Ippolito, B. LaBombard, B. Lipschultz, J. R. Myra, J. L. Terry and S. J. Wukitch, Plasma Phys. Control. Fusion **56**, 015004 (2014).

[11] K. Crombé, R. D'Inca, J. Jacquot, R. Ochoukov, M. Usoltceva, A. Kostic, F. Louche, D. Van Eester, A. Nikiforov, J. Moreno, S. Heuraux, S. Devaux, J. Moritz, E. Faudot, H. Fünfgelder, H. Faugel, F. Zeus and J-M. Noterdaeme, "IShTAR: a helicon plasma source to characterise the interactions between ICRF and plasma," 26th IAEA Fusion Energy Conference, Kyoto, Japan, 17-22 October 2016, IAEA-CN-234/EX-P6-48.

[12] M. Martin, W. Gekelman, P. Pribyl, B. Van Compernolle, T. Carter, D. Van Eester, K Crombé, "Experimental Study of Convective Cells and RF Sheaths Excited by a Fast Wave Antenna in the LAPD," Bull. American Phys. Soc. **61**, 299, paper PP10-11.

[13] L. Colas, J. Jacquot, S. Heuraux, E. Faudot, K. Crombé, V. Kyrytsya, J. Hillairet and M. Goniche, Phys. Plasmas **19**, 092505 (2012).

[14] D. N. Smithe, D. A. D'Ippolito, and J. R. Myra, AIP Conference Proceedings **1580**, 89 (2014).

[15] N. Bertelli, E.F. Jaeger, J.C. Hosea, C.K. Phillips, L. Berry, S.P. Gerhardt, D. Green, B. LeBlanc, R.J. Perkins, P.M. Ryan, G. Taylor, E.J. Valeo and J.R. Wilson, Nucl. Fusion **54**, 083004 (2014).

[16] D. Van Eester, K. Crombé and V. Kyrytsya, Plasma Phys. Control. Fusion **55**, 055001 (2013).

[17] J.R. Myra and D.A. D'Ippolito, Plasma Phys. Controlled Fusion **52**, 015003 (2010).

[18] H. Kohno, J. R. Myra, and D. A. D'Ippolito, Phys. Plasmas **19**, 012508 (2012).

[19] D. A. D'Ippolito, J. R. Myra, R. Ochoukov, and D. G. Whyte, Plasma Phys. Control. Fusion **55**, 085001 (2013).

[20] H. Kohno, J. R. Myra, and D. A. D'Ippolito, Phys. Plasmas **20**, 082514 (2013).

[21] J. R. Myra and D. A. D'Ippolito, Phys. Plasmas **22**, 062507 (2015).

[22] J. R. Myra, Phys. Plasmas **24**, 072507 (2017).

[23] K. Takayama, H. Ikegami, and S. Miyazaki, Phys. Rev. Lett. **5**, 238 (1960).

[24] R. L. Stenzel, Phys. Rev. Lett. **60**, 704 (1988).

[25] H. Kohno and J. R. Myra, Comput. Phys. Commun. **220**, 129 (2017).

[26] The quantity with dimensions of impedance is actually $z_S A_n$ where A_n is the surface area. Therefore z_S is more correctly referred to as a sheath impedance parameter; however, for brevity we will continue to refer to it as the "sheath impedance" implicitly considering unit area A_n.

[27] H. Kohno, J. R. Myra, and D. A. D'Ippolito, Phys. Plasmas **22**, 072504 (2015) and errata in Phys. Plasmas **23**, 089901 (2016).

[28] H. Kohno and J. R. Myra, Phys. Plasmas 26, 022507 (2019).

[29] J. R. Myra and H. Kohno (2018). "Radio frequency wave interactions with a plasma sheath: the role of wave and plasma sheath impedances" Zenodo. http://doi.org/10.5281/zenodo.2533415

[30] T. H. Stix, *Waves in Plasmas*, (Springer-Verlag, New York, 1992).

Figure Captions

Fig. 1. Geometry of the model showing an incident (right-propagating) wave (subscript 1) and a reflected (left-propagating) wave (subscript 2) on a semi-infinite domain. The sheath boundary condition is imposed at the right side of the domain and the magnetic field is at an oblique angle to the sheath. The model is periodic in the y and z directions. In this paper the magnetic field **B** is in the x-y plane.

Fig. 2. Variation of the dimensionless sheath impedance with dimensionless wave frequency. Other parameters are $b_x = 0.2$, $\hat{\Omega} = 0.1$, $\xi = 10$. Some structure is seen at the ion plasma frequency $\hat{\omega} = 1$ and at the ion cyclotron frequency $\hat{\omega} = \hat{\Omega} = 0.1$. See Ref. 22 for a detailed explanation. [Associated dataset available at https://doi.org/10.5281/zenodo.2533415] (Ref. 29).

Fig. 3. Properties of the electrostatic slow wave for the parameters $\varphi = 0.4$, B = 2 T, $\omega = 2\Omega_i$, $k_y = 0.2$/cm, $k_z = 1.6$/cm, $\xi = 20$. Shown are: (a) the solution of the dispersion relation for k_x, (b) the corresponding x-component of the group velocity, and (c) the sheath to wave impedance ratio defined by Eq. (8). In these plots Re (Im) parts are shown as solid (dashed) lines and the color scheme is consistent across all the panels. The incoming branch is labeled and shown in red. [Associated dataset available at https://doi.org/10.5281/zenodo.2533415] (Ref. 29).

Fig. 4. Contours of |A| in the plane of density and magnetic field angle near the lower hybrid resonance density ($\log_{10} n_{eLH}/cm^3 = 10.5$) for the parameters B = 2 T, $\omega = 2\Omega_i$, $T_e = 15$ eV, $k_y = 0.2$/cm, $k_z = 1.6$/cm, $\xi = 20$. Small φ corresponds to grazing incidence. For $n_e < n_{eLH}$, contours are labeled by power absorption percentage f_p; for $n_e > n_{eLH}$ contours are labelled by |A|. [Associated dataset available at https://doi.org/10.5281/zenodo.2533415] (Ref. 29).

Fig. 5. Variation of |A| with density for $\varphi = 0.15$ radians, i.e. a cut of Fig. 4 over a larger range of densities. Other parameters are the same as in Fig. 4. The thin gray line indicates the lower hybrid resonant density where $\varepsilon_\perp = 0$. [Associated dataset available at https://doi.org/10.5281/zenodo.2533415] (Ref. 29).

Fig. 6. Upper panels: maximum (solid line) and average (dashed line) values over density and angle of f_p and |A| vs. k_y. Lower panels: the density in units of 10^{11} cm^{-3} and angle at which the maxima occur for f_p (black line) and |A| (red line). A thin gray line marks the LH resonant density. See the text for base case parameters and additional discussion. [Associated dataset available at https://doi.org/10.5281/zenodo.2533415] (Ref. 29)

Fig. 7. Real (solid) and imaginary (dashed) parts of ρ for the case $\omega = 20\ \Omega_i$ with all other parameters at their base case values and $\varphi = 0.4$, $k_y = 0.2$. The two sets of lines are for the two branches, incoming and outgoing, with incoming shown in red. [Associated dataset available at https://doi.org/10.5281/zenodo.2533415] (Ref. 29).

Fig. 8. Maximum values over density and angle of f_p (upper panel) and |A| (lower panel) vs. k_y for the four cases discussed in the text. Note that |A| is only shown for the cases that admit an evanescent SW solution. [Associated dataset available at https://doi.org/10.5281/zenodo.2533415] (Ref. 29).

Fig. 9. Sample rfSOL domain and solution showing Im $E_{||}/K_{max}$ for the parameters $n_e = 1\times10^{18}$ m^{-3}, $B_{0x} = 4$ T, $k_z = 40$ /m, $\omega/2\pi = 80$ MHz, $T_e = 15$ eV and $K_{max} = 5$ kA/m. The dark black line at x = 2.26 m is the RF antenna. The sheath boundary condition is applied on the wall with the bump at the right end of the domain. [Associated dataset available at https://doi.org/10.5281/zenodo.2533415] (Ref. 29).

Fig. 10. Real (solid) and imaginary (dashed) parts of ρ for $k_z = 160$/m (blue), 80/m (green) and 40/m (red). The sheath-plasma resonance occurs at $\rho = 1$. The two sets of lines for each case are for the incoming and outgoing branches. For each k_z, the outgoing branch, j = 2 in the notation of Sec. II A, is the one with a positive real part leading to resonant behavior in Eq. (7). [Associated dataset available at https://doi.org/10.5281/zenodo.2533415] (Ref. 29).

Fig. 11. Spatial structure along the sheath surface of various quantities: RF sheath voltage (upper), sheath impedance (middle) and normal displacement D_n proportional to sheath current density (lower) for $k_z = 40$ m^{-1} (left) and 160 m^{-1} (right). Results are shown for a sequence of values of antenna driving current K_{max}. See Fig. 9 for the simulation geometry. [Associated dataset available at https://doi.org/10.5281/zenodo.2533415] (Ref. 29).

Fig. 12. Maximum values of normalized sheath voltage ξ_{max} vs. antenna current K_{max} for k_z = 40, 80 and 160 m^{-1}. The arrows indicate the approximate locations of the large slope regions of the curves, from which the corresponding values of ξ_{max} may be ascertained. [Associated dataset available at https://doi.org/10.5281/zenodo.2533415] (Ref. 29).

Fig. 13. Electrostatic (solid) and electromagnetic (dashed) results for Re A, Im A and |A| for the cases k_z = 160/m (red), 20/m (blue), 0/m (black). Note that for small $\mathbf{k}_t$ the sheath becomes conducting ($A \to -1$) while for large $\mathbf{k}_t$ it is quasi-insulating ($A \to 1$). [Associated dataset available at https://doi.org/10.5281/zenodo.2533415] (Ref. 29).

This manuscript was accepted by Phys. Plasmas. Click here to see the version of record.

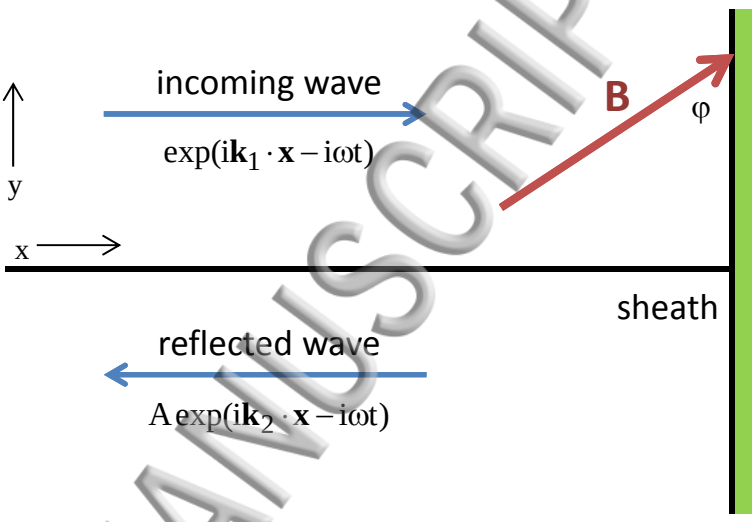

This manuscript was accepted by Phys. Plasmas. Click here to see the version of record.

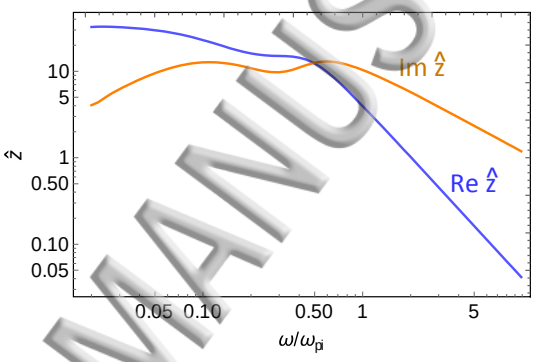

This manuscript was accepted by Phys. Plasmas. Click here to see the version of record.

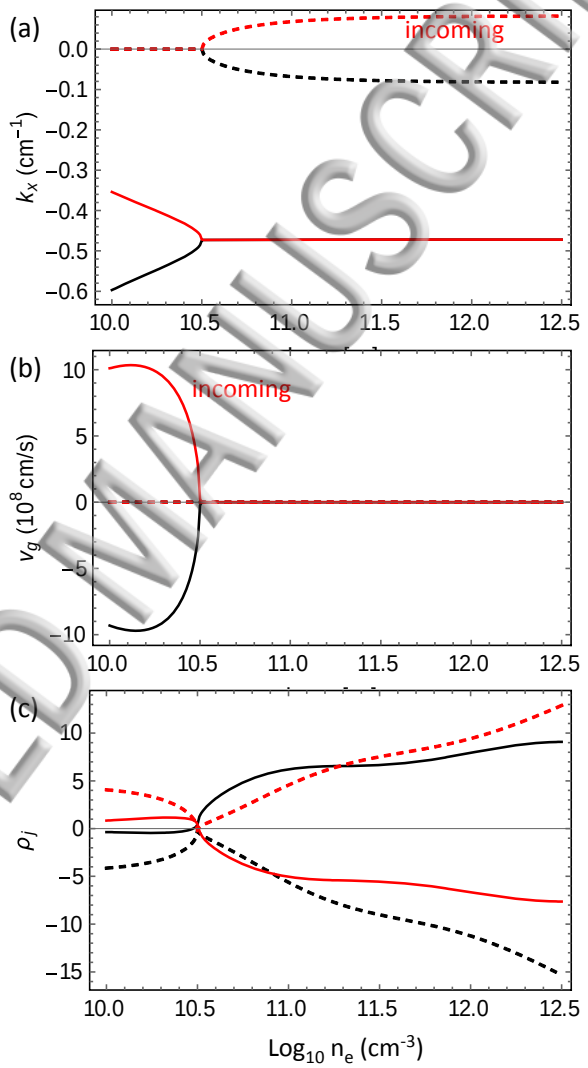

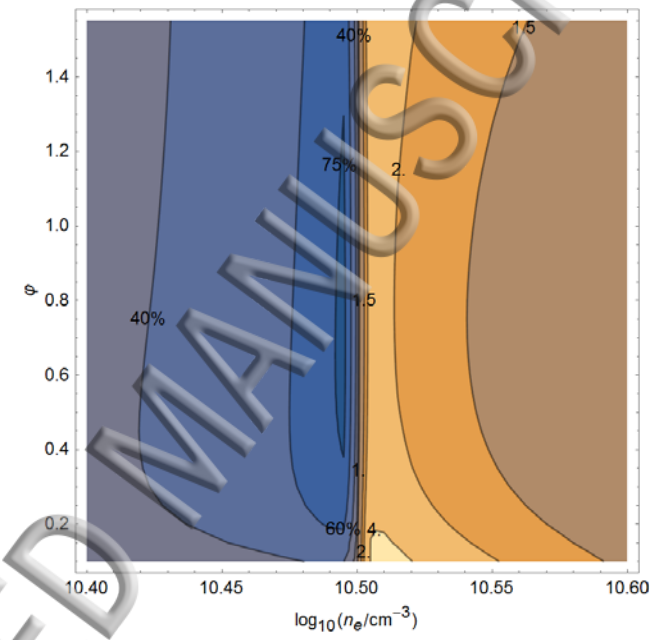

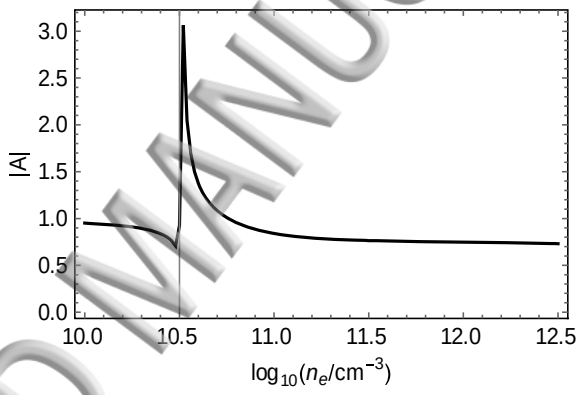

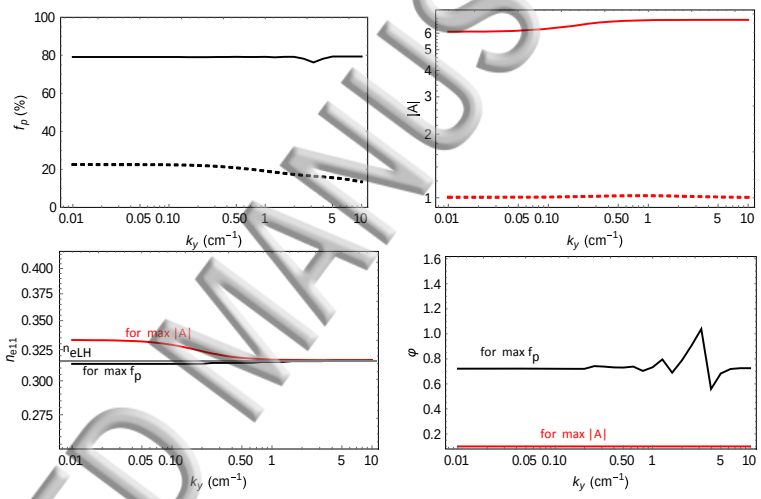

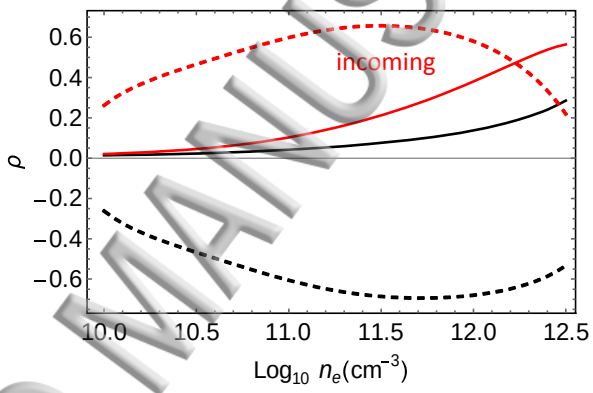

This manuscript was accepted by Phys. Plasmas. Click here to see the version of record.